

See discussions, stats, and author profiles for this publication at: <https://www.researchgate.net/publication/263978581>

# Influence of Hydrated Silica Surfaces on Interfacial Water in the Presence of Clathrate Hydrate Forming Gases

ARTICLE in THE JOURNAL OF PHYSICAL CHEMISTRY C · NOVEMBER 2012

Impact Factor: 4.77 · DOI: 10.1021/jp305529d

---

CITATIONS

10

---

READS

52

## 4 AUTHORS, INCLUDING:



[S. Alireza Bagherzadeh](#)

University of British Columbia - Vancouver

10 PUBLICATIONS 109 CITATIONS

[SEE PROFILE](#)



[Peter Englezos](#)

University of British Columbia - Vancouver

171 PUBLICATIONS 4,786 CITATIONS

[SEE PROFILE](#)



[John A. Ripmeester](#)

National Research Council Canada

713 PUBLICATIONS 15,630 CITATIONS

[SEE PROFILE](#)

# Influence of Hydrated Silica Surfaces on Interfacial Water in the Presence of Clathrate Hydrate Forming Gases

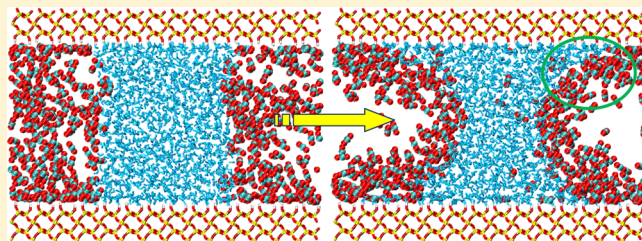
S. Alireza Bagherzadeh,<sup>†</sup> Peter Englezos,<sup>\*,†</sup> Saman Alavi,<sup>\*,‡</sup> and John A. Ripmeester<sup>\*,‡</sup>

<sup>†</sup>Department of Chemical and Biological Engineering, University of British Columbia, Vancouver, British Columbia, V6T 1Z3, Canada

<sup>‡</sup>Measurement Science and Standards, National Research Council of Canada, Ottawa, Ontario, K1A 0R6, Canada

## Supporting Information

**ABSTRACT:** We study the hydrated silica–water interface in the presence of methane or carbon dioxide gas with molecular dynamics simulations. The simulations are performed with a limited amount of water, which forms a meniscus between two hydroxylated silica surfaces separated by 40 to 60 Å. Simulations were performed with the remaining space of the simulation cell left empty or filled with different numbers of methane or carbon dioxide gas molecules. The meniscus is used to determine the contact angle between water and silica in the absence and presence of the gases. The distribution profiles of the water and gas phases are determined over the duration of the simulation. The water number density in the layers adjacent to the silica is higher, and these layers are more structured and less mobile compared with water layers far from the surface. Additionally, the concentrations of the gases are significantly higher at the liquid and silica interfaces than in other locations in the gas phase. We speculate that the enhanced concentration of gases at the interface along with the extended contact area (curved meniscus compared with flat interface in the absence of silica surfaces) between water and guest molecules at the meniscus as well as lesser mobility of water molecules near the silica surface may provide a mechanism for the heterogeneous nucleation of the clathrate hydrate in water-wetting porous medium.



## ■ INTRODUCTION

The formation mechanism of methane clathrate hydrate in natural deposits is important from both industrial and fundamental scientific points of view. No conclusive mechanism is as yet available for the formation of vast naturally occurring methane hydrate reserves. The industrial implications of understanding and controlling hydrate processes include the synthesis of methane hydrate from methane gas and water for storage and transportation purposes,<sup>1,2</sup> extraction of methane from natural methane hydrate formations in permafrost and ocean sediments,<sup>3</sup> and sequestration of carbon dioxide in depleted gas reservoirs.<sup>4</sup>

The main difficulty in synthesizing methane hydrate is bringing methane gas and liquid water into contact at appropriate molecular ratios so as to form the clathrate hydrate phase. The solubility of methane gas in water is extremely low, with the saturated methane aqueous solution mole fraction of  $2.55 \times 10^{-5}$  at  $25^\circ\text{C}/0.1 \text{ MPa}$ <sup>5</sup> and  $1.14 \times 10^{-3}$  at  $3^\circ\text{C}/3.37 \text{ MPa}$  (near hydrate formation conditions),<sup>6</sup> whereas methane mole fraction in the clathrate hydrate phase is 0.142.<sup>7</sup> Therefore, the concentration of methane in a saturated aqueous solution is at least  $\sim 125$  times smaller than required for hydrate formation. This difference in concentration between the saturated solution and clathrate hydrate phase is less pronounced for the  $\text{CO}_2$  hydrate as the carbon dioxide mole fraction in the saturated solution at  $25^\circ\text{C}/1 \text{ MPa}$  is  $6.09 \times 10^{-4}$ <sup>8</sup> and the mole fraction in the saturated solution at  $3^\circ\text{C}/$

$1.42 \text{ MPa}$  (near the hydrate equilibrium point) is 0.0155.<sup>9</sup> In the hydrate phase, the  $\text{CO}_2$  mole fraction is 0.139.<sup>8</sup>

Presently, industrial and engineering lab hydrate synthetic methods often involve the production of fine water jets, which are sprayed in saturated methane gas environments.<sup>10</sup> This method increases the contact of water and methane gas, enhancing the rate of hydrate formation. The other common method for synthesizing hydrates involves exposing water surfaces, aqueous solution surfaces, water/organic interfaces, or water saturated sand-beds to high pressures of methane gas.

The phenomenon of hydrate formation becomes more complex when the water and gas phases are in contact with a solid surface or porous environments, such as silica sand beds or porous silica gel.<sup>11,12</sup> The nature of the interactions between the water, gas-phase guest, and solid substrate phases must be understood to gain more insight about the fundamentals of this process. Because these interactions mostly occur at the interface between the phases and usually extend over nanoscale lengths, the investigation of such systems using molecular simulation approaches is feasible and can give rise to useful insights into the process of hydrate formation.

Because sandy reservoirs have the highest saturation of hydrates,<sup>13</sup> we use silica as the porous surface in our

Received: June 5, 2012

Revised: November 2, 2012

Published: November 7, 2012



simulations. A study of the interaction between water and the silica surface, especially when the gas-phase guest molecules are present, can help in understanding the state of the system before the onset of nucleation of hydrates.

Pure silica (taken to be the quartz phase) has the molecular formula  $\text{SiO}_2$ , but adjacent to water surfaces, the outer layer of Si atoms is considered to be hydroxylated. Argyris et al.<sup>14</sup> analyzed the structure and dynamics of interfacial water on silica with different densities of hydroxyl group on the surface. They found that up to  $\sim 14$  Å away from the surface, the local water has different structural and dynamical characteristics from bulk water. Experimental techniques including IR spectroscopy,<sup>15</sup> differential scanning calorimetry,<sup>16</sup> thermoporometry,<sup>17</sup> DSC, and FTIR<sup>18</sup> have been utilized to prove the existence of a special nonfreezable state of water of thickness from 3 to 15 Å<sup>19</sup> on different types of substrate such as quartz, clayey silt, silica gel, and hydrophilic polymers.

Many methane hydrate formation simulation studies use a homogeneous nucleation mechanism with some type of methane delivery, usually in the form of artificially supersaturated methane solutions to study the methane hydrate formation mechanism.<sup>20–24</sup> These simulations are useful in providing insight into the structures of hydrate nuclei that form in solution and the growth of hydrate after nucleation. However, supersaturation of the aqueous solution with respect to methane may alter the hydrate formation mechanism compared with the mechanism that actually occurs in nature. Other studies simulate the hydrate formation process in the presence of silica walls to mimic the natural conditions of hydrate formation in sediments. Such simulations have been performed for  $\text{CO}_2^{25}$  and  $\text{CH}_4$  hydrate.<sup>26</sup>

To gain insight into the heterogeneous hydrate nucleation process in the presence of silica surfaces, we study the structure of the water meniscus between two hydroxylated silica surfaces (a slit-like pore) and under vacuum, methane, or carbon dioxide atmospheres. We study the structure of the silica/water/gas interfaces and determine if these sites have potential as nucleation sites for hydrate formation.

## COMPUTATIONAL METHODS

The molecular dynamics (MD) simulations were run with the DL\_POLY<sup>27</sup> program version 2.20. The intermolecular potential for atoms on different molecules is considered as a sum of Lennard-Jones and Columbic interactions with force-field parameters summarized in Table 1. A united-atom potential was used for methane,<sup>28</sup> the EPM potential was used for  $\text{CO}_2$ ,<sup>29</sup> the TIP4P-ice potential was used for water,<sup>30</sup>

and the potential of Lopes et al.<sup>31</sup> was employed to represent the silica atomic interactions. Standard combination rules were used to calculate the Lennard-Jones parameters for the unlike pairs of atoms,  $\epsilon_{ij} = (\epsilon_i \epsilon_j)^{1/2}$  and  $\sigma_{ij} = (\sigma_{ii} + \sigma_{jj})/2$ . These combinations of potentials have been used in simulations of methane and carbon dioxide clathrate hydrate nucleation and decomposition<sup>32,33</sup> and are successful in capturing physical features of clathrate hydrate systems. Recently, custom-designed methane–water<sup>34–36</sup> and  $\text{CO}_2$ –water<sup>37</sup> interaction potentials have been used in simulations of methane and carbon dioxide hydrates. These potentials will likely give better quantitative agreement between simulation predictions and experiments in the context of hydrate simulations. However, because we do not have custom-designed parameters for the water–silica and gas–silica surfaces, we have used the simple combination rules mentioned above to determine Lennard-Jones parameters for interactions between different molecules in the simulation.

The cutoff radius for all of the interatomic interactions in the simulation box was set to 15 Å, and the long-range Columbic interactions were treated using the Ewald summation method. All simulations were performed in the Nosé–Hoover version of the NVT ensemble with the thermostat constant of 0.2 ps and initial pressure of 1 bar. The equations of motion were integrated every 1 fs with the total time of 2 ns. Periodic boundary conditions were applied in all three dimensions, with vacuum gaps separating images of the system in the  $y$  direction.

The crystallographic unit cell of silica (quartz)<sup>38</sup> is used to construct the silica layers. Surface silica atoms potentially exposed to water were hydroxylated using an O–H bond length of 1.1 Å, according to setup of Lopes et al.<sup>31</sup> The details of the construction of silica are given elsewhere.<sup>39</sup> The two silica slabs are placed in the simulation box in the  $xz$  plane (38.6 Å apart along the  $y$  axis). Variable numbers of water molecules (from 432 to 1584) were placed between the silica slabs in an initially parallelepiped configuration. The maximum number of 1584 water molecules initially occupied about half of the simulation cell along the  $z$  direction. In simulations with methane and carbon dioxide, gas molecules were placed in the remaining empty space of the simulation box, surrounding the water phase from both sides along the  $z$  direction. Two sets of simulations were performed at 275 and 300 K. Two simulations for methane in contact with the water meniscus are performed with silica slab separations of 50 and 62 Å (in the  $y$  direction) to study the effect of slab separation on the meniscus and water properties. The numbers of molecules in each simulation and the numbering scheme used to represent the different simulations are given in Table 2. The atoms of the silica slabs are kept frozen during the simulations. The initial setup and final configuration of the simulation cell at 275 K with 1584 water molecules are shown in Figure 1. The shape of the meniscus shows that water has wetted the silica surface, indicating that it is hydrophilic.

To characterize the distribution of water molecules, the space between the silica surfaces is binned into volume elements of 1 Å length in  $yz$  plane and a depth equal to the length of the simulation box along the  $x$  axis (i.e., 39.328 Å). The silica–water and water–gas (water–vacuum) boundaries are found by determining the average water number densities in the bins over the trajectory of the simulation. The distribution of water molecules in the form of a meniscus is shown in Figure 2. The outer boundary of the water phase is not sharp, and the density of water decreases gradually from  $\sim 1 \text{ g}\cdot\text{cm}^{-3}$  in the water phase

**Table 1. Force-Field Parameters: The Atomic Partial Charges and Lennard-Jones Parameters**

atom	$\epsilon$ (kJ·mol <sup>-1</sup> )	$\sigma$ (Å)	$q$ (e)	ref
C ( $\text{CH}_4$ )	1.3650	3.6400	0	27
C ( $\text{CO}_2$ )	0.2411	2.7850	0.6645	28
O ( $\text{CO}_2$ )	0.6901	3.0640	-0.33225	
O ( $\text{H}_2\text{O}$ )	0.8822	3.1668	0	29
E ( $\text{H}_2\text{O}$ )	0	0	-1.1794	
H ( $\text{H}_2\text{O}$ )	0	0	0.5897	
Si ( $\text{SiO}_2$ -bulk)	2.5104	3.9200	1.08	30
O ( $\text{SiO}_2$ -bulk)	0.6364	3.1538	-0.53	
O ( $\text{SiO}_2$ -surface)	0.6364	3.1538	-0.64	
H ( $\text{SiO}_2$ -surface)	0.1925	0.4000	0.32	

**Table 2.** Temperature (K), Number of Molecules in the Water and Gas Phases, Measured Contact Angles (Degrees), and Components of the Pressure Tensor (Bar) in the Simulations Performed in This Work<sup>a</sup>

simulation no.	T	number of molecules		contact angle	$P_{xx}$	$P_{yy}$	$P_{zz}$
		H <sub>2</sub> O	gas				
1	275	432	0	38.3 ± 2.8	208.9	-644.5	197.9
2		1584	0	27.3 ± 3.6	-96.8	-430.0	-26.6
3		1584	306 (CH <sub>4</sub> )	36.7 ± 4.5	-22.6	-612.0	58.4
3a		1920	375 (CH <sub>4</sub> )	36.8 ± 7.3	-8.8	-570.4	104.0
3b		2400	461 (CH <sub>4</sub> )	39.8 ± 1.2	-13.0	-462.2	99.4
4		1584	612 (CH <sub>4</sub> )	51.1 ± 7.2	118.4	-663.0	193.2
5		1584	306 (CO <sub>2</sub> )	39.0 ± 7.0	-27.5	-620.6	28.0
6		1584	459 (CO <sub>2</sub> )	52.4 ± 5.7	22.8	-662.4	66.4
7	300	864	0	32.6 ± 4.2	-22.5	-507.4	30.6
8		1584	0	22.5 ± 4.2	-35.8	-329.0	-78.4
9		1584	306 (CH <sub>4</sub> )	28.5 ± 6.0	-136.2	-510.9	41.5
10		1584	918 (CH <sub>4</sub> )	34.1 ± 4.1	418.8	-278.5	509.8
11		1584	306 (CO <sub>2</sub> )	29.9 ± 1.0	-41.1	-532.9	5.9
12		1584	459 (CO <sub>2</sub> )	31.9 ± 5.2	5.0	-562.0	37.4

<sup>a</sup>Simulations all have total run time of 2 ns.

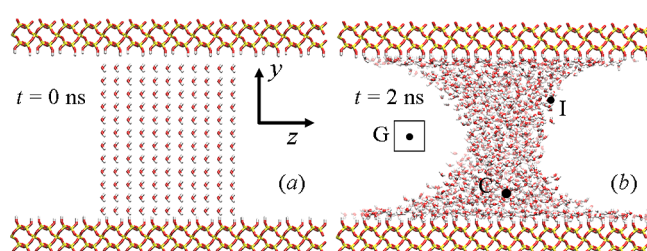


**Figure 1.** (a) Initial setup and (b) final configuration for simulation (2) at 275 K with 1584 water molecules between the silica slabs at the top and bottom of the simulation cell. The formation of the meniscus illustrates the hydrophilic character of the silica surfaces used in this work.

to 0 as we move away from the water phase. To calculate the contact angle,  $\alpha$ , between the water and hydroxylated silica phase, the outer boundary of water phase is chosen as sites where the density has the mean value of 0.5 g/cm<sup>3</sup>. In all cases, ~2.5 Å arc of the meniscus near the silica surface was used to draw a straight tangent line, as illustrated in Figure 2, which yielded an  $r^2$ -value of >0.98. The average of the tangents at the four points of contact of the meniscus with the silica surface is used. This method is similar to the direct observation method of Saville.<sup>40</sup> Energy-based methods have also been used to determine the contact angle.<sup>40,41</sup>

The structure of the water phase along the  $y$  direction of the simulation cell (perpendicular to the silica surfaces) is determined by calculating the average water molecule distribution over the final 1 ns of the trajectory where the shape of the meniscus has stabilized. The profile of the relative number of water molecules as we move perpendicular to the silica surfaces is shown in Figure 3 along with a typical snapshot from the simulation. Analyses are performed on three 3 Å thick layers of water molecules. These layers, shown in Figure 3, represent the bound water adjacent to the silica surface ( $L_1$ ), a water layer adjacent to the first layer ( $L_2$ ), and the water layer near the center of the simulation cell far from the silica surface (C). The peaks of enhanced water density close to each silica surface (roughly within  $L_1$  and  $L_2$ ) show the formation of two distinct hydration layers near the surface. Beyond these layers, the number of water molecules decreases toward the center,

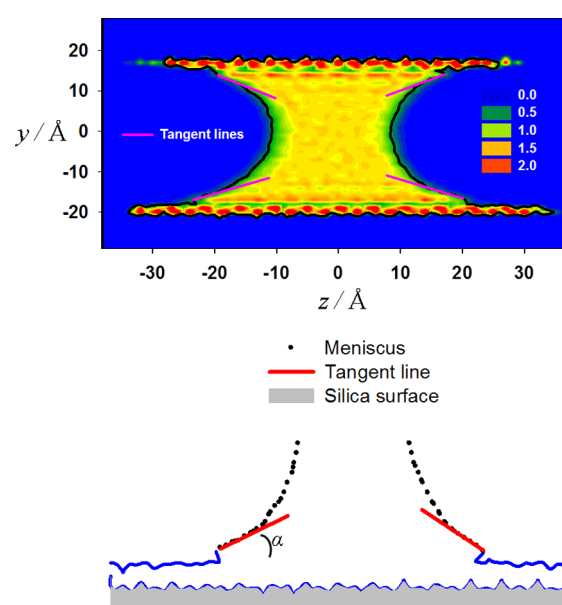


**Figure 2.** Typical distribution of water molecules between the silica surfaces from binning areas in the  $yz$  plane of the simulation (2). The higher local concentration of water molecules near the silica surfaces is apparent. The outer boundary of the water meniscus is used to estimate the contact angle. Four tangent lines were drawn on four points of contact of water to the silica surfaces, and the contact angles are reported in Table 2. A schematic of the method for drawing tangent lines on the meniscus to determine the contact angle is shown in the bottom panel. An arc of approximate length of 2.5 Å is used to draw the tangent to the meniscus near the silica surface.

with little indication of further water-layer structuring. The decrease in the number of water molecules as we move away from the surface is due to the shape of the meniscus.

The  $F_3$ -order parameter of Baez and Clancy<sup>42</sup> is used to characterize the local arrangement of water molecules at different locations during the simulation. The  $F_3$  parameter is based on the value of 104.25° for the O–O–O angle observed in tetrahedral arrangement of the oxygen atoms of water in solid ice phases

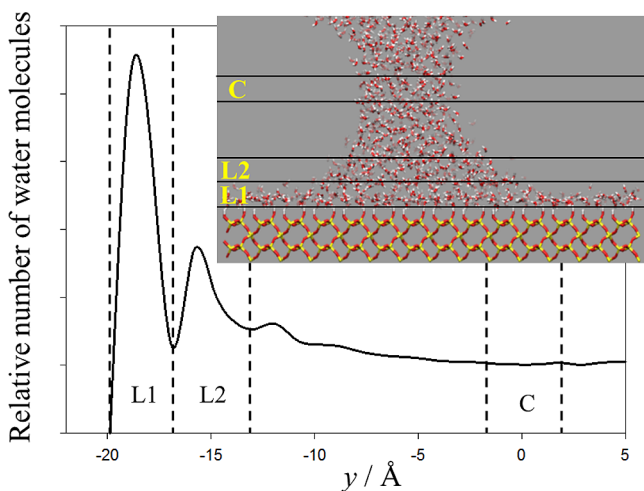


**Figure 3.** Water distribution along the distance between the two silica surfaces. Two major peaks are present near the surface. For clarity, only half of the symmetric profile is shown.

$$F_{3,i} = \langle [\cos \theta_{jik} |\cos \theta_{jik}| + \cos^2 104.25]^2 \rangle_{j,k}$$

$$= \begin{cases} \sim 0.1 \text{ liquid water} \\ \sim 0.0 \text{ solid water (ice, hydrate)} \end{cases} \quad (1)$$

Here  $\theta_{jik}$  is the angle between triplets of oxygen atoms with the  $i$ th atom being in the center and the  $j$  and  $k$  oxygen atoms within a spherical shell of radius 3.5 Å around atom  $i$ . This distance corresponds to the first minimum in the radial distribution function of O–O pairs of water molecules in liquid water phase.

The orientations of water molecules were studied by characterizing the angle between the water dipole moment vector ( $\mathbf{M}$ ) and the normal to the silica surface,  $\mathbf{n}$  (0,1,0); see Figure 4. The average value of the cosine of this angle,  $\varphi$ , for each layer is calculated.

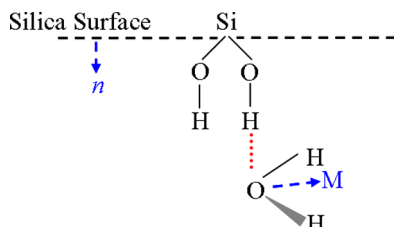


**Figure 4.** Schematic of the orientation of water molecules in the layer adjacent to the silica surface. The blue dotted arrow shows the direction of dipole moment vector  $M$  and the vector normal to the silica surface,  $n$ .

A residence correlation function,<sup>14</sup>  $C_R$ , is defined to study the exchange and dynamics of water molecules in each layer

$$C_R = \frac{\langle O_w(t)O_w(0) \rangle}{\langle O_w(0)O_w(0) \rangle} \quad (2)$$

where  $O_w(t)$  is an index, assigned a value of 0 if the water molecule oxygen atom has moved outside the layer it occupied at time  $t = 0$  and a value of 1 if the water molecule oxygen atom has remained inside its corresponding  $t = 0$  layer. The value of  $C_R$  decays from 1 to 0 as water molecules translate and exchange between layers during the course of simulation.

The intermittent hydrogen-bond correlation function,<sup>14b</sup>  $C(t)$ , is defined to inspect the rate of hydrogen-bond formation and decay

$$C(t) = \frac{\langle H(t) \cdot H(0) \rangle}{\langle H(0) \cdot H(0) \rangle} \quad (3)$$

If two water molecules are hydrogen-bonded at time  $t$ , then we assign  $H(t) = 1$  to that pair; otherwise,  $H(t) = 0$ . We continue checking the hydrogen bonding of each particular pair throughout the trajectory, and the number of hydrogen bonds is counted, and the average value is calculated for different water layers at each time step.

## RESULTS AND DISCUSSION

Snapshots of the simulation with the water meniscus in contact with  $\text{CH}_4$  or  $\text{CO}_2$  gas at 275 and 300 K are shown in Figure 5.

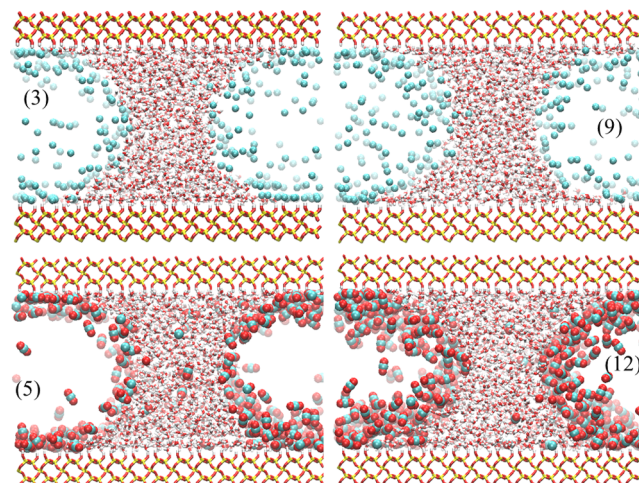


**Figure 5.** Final ( $t = 2$  ns) snapshot of the simulations at  $T = 275$  (simulations 3 and 5 of Table 2) and  $300$  K (simulations 9 and 12 of Table 2) in the presence of  $\text{CH}_4$  or  $\text{CO}_2$  gaseous phases. The  $\text{CH}_4$  molecules are illustrated as cyan spheres and  $\text{CO}_2$  as linear cyan–red molecules. The enhanced concentrations of the gases near the interfaces are clearly visible.

The initial setup configurations for these simulations, which have uniform gas distribution, are shown in Figure S1 of the Supporting Information. The concentration enhancement of methane and carbon dioxide on the water meniscus and silica interfaces is striking and is quantified below. As expected, water spreads to a greater extent on the silica surface at the higher temperature. There is some solubility for  $\text{CO}_2$  in the water phase, but very little methane is dissolved in the water phase. For reference, a set of simulations of a flat bulk water surface in contact with methane and carbon dioxide gas are performed under similar simulation conditions. A sample snapshot of the water/gas distribution in these systems is shown in Figure S2 of the Supporting Information.

**Water and Gas Distribution.** After the meniscus has stabilized, the number of water oxygen atoms and gas carbon atoms in each bin in the simulation cell are determined, and the results are averaged over the second nanosecond of the trajectory production run. Three-dimensional density plots for the concentration of the species in different parts of the simulation cell are calculated, and samples are shown in Figure 6 for simulation #3 of Table 2. The enhanced concentration of water molecules at the silica surface and the enhanced

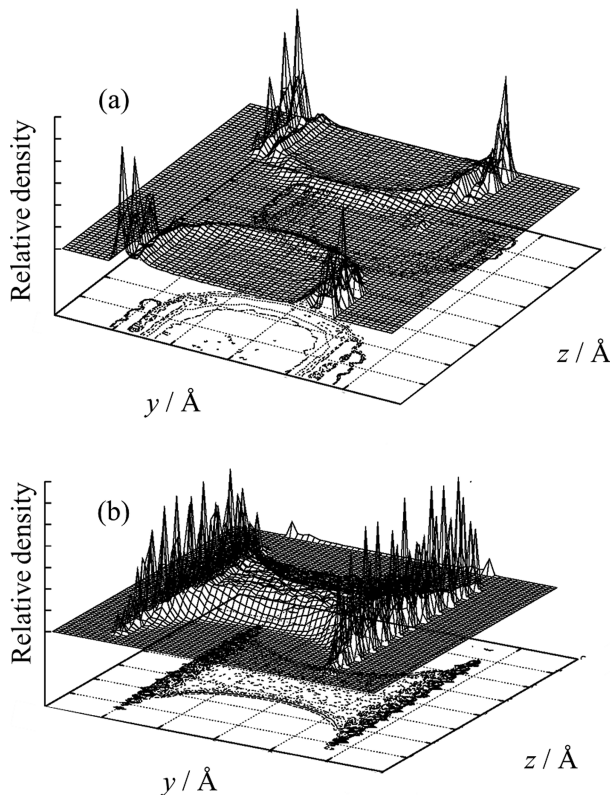


**Figure 6.** Concentration surfaces for (a) methane and (b) water density projected on the  $yz$  plane at 275 K. The enhanced concentrations of methane at the silica surface–gas and water–gas interfaces can be observed. Water density is also enhanced at the silica surface.

concentration of methane gas molecules at the water and silica interfaces are clearly visible in these Figures. The high density loci near the surface, seen in Figures 2 and 6b, correspond to the locations of surface O–H groups of silica. Water molecules near the silica surface make strong hydrogen bonds with these O–H groups and are preferentially located at these locations.

In Figure 6a, we see that methane concentration is enhanced at the water surface, but enhancement is even greater on segments of the silica surface not covered with water. It is experimentally observed that for unstirred liquid  $\text{CO}_2$ , propane, and isobutane phases in contact with liquid water under high pressures, spontaneous macroscopic hydrate formation is triggered by the adsorption of guest molecules on the water–guest interface.<sup>43</sup> Similar behavior was observed for gas-phase Xe. However, X-ray diffraction and reflectivity measurements of Lehmkühler et al.<sup>44</sup> for the gaseous  $\text{CO}_2$ –liquid water system showed the formation of a thin film of liquid-like  $\text{CO}_2$  on the water interface but the absence of hydrate formation. We are currently running longer simulations at lower temperatures to observe the possible nucleation of hydrates in silica pores.

The concentration of the gases on the interface and in the gas phase are calculated and given for the different simulations in Table 3. We observe a notable density enhancement of methane and carbon dioxide at the site of the meniscus. Carbon dioxide is enhanced on the surface to a greater degree than methane.

For reference, the density profile of bulk water in contact with methane/carbon dioxide phases through a flat interface is given in Figure 7. A similar density enhancement of the gas

**Table 3. Density of  $\text{CH}_4$  and  $\text{CO}_2$  Molecules at the Interface and Gas Phase of the Simulation Cell for Different Simulation Setups**

simulation (gas)	gas density ( $\text{mol}\cdot\text{cm}^{-3}$ )		
	G (gas phase)	I (water–gas interface)	ratio (I/G)
3 ( $\text{CH}_4$ )	0.002	0.006	2.23
4 ( $\text{CH}_4$ )	0.009	0.008	0.85
5 ( $\text{CO}_2$ )	0.000	0.007	13.72
6 ( $\text{CO}_2$ )	0.001	0.009	10.68
9 ( $\text{CH}_4$ )	0.003	0.005	1.47
10 ( $\text{CH}_4$ )	0.020	0.011	0.54
11 ( $\text{CO}_2$ )	0.001	0.006	6.42
12 ( $\text{CO}_2$ )	0.002	0.009	4.52

molecules at the water interface is seen in these simulations as well.

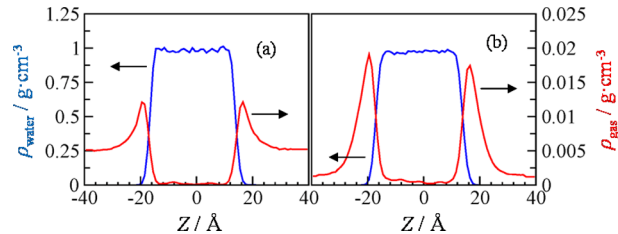


**Figure 7.** Distribution of hydrate forming gases adjacent to the water interface along the length of simulation box (no silica surface) for (a) the methane–water system and (b) the carbon dioxide–water system. The behavior of the methane–water system is similar to that of Figure 5.

**Contact Angle.** The average values of the contact angle between the water and silica phases in different simulations are given in Table 2. Snapshots of the final configurations of the water/ $\text{CH}_4$  and water/ $\text{CO}_2$  systems at two temperatures are shown in Figure 5. Comparing the snapshots shows that at the lower temperature, the curvature of the meniscus decreases, and water spreads less on the hydrophilic surface; therefore, the contact angle increases. This is consistent with the fact that the surface tension of SPC/E water increases from 61.3 to 64.5 mN/m as temperature decreases from 300 to 275 K.<sup>45</sup> The presence of methane and  $\text{CO}_2$  molecules on the gas phase affects the contact angle. For each gas, the greater gas pressure leads to larger water–silica contact angles. The  $\text{CO}_2$  gas with its higher solubility leads to smaller contact angles than similar simulation with  $\text{CH}_4$  gas.

It should be noted that the contact angle is a property of a bulk sample of water. In simulations where the number of water molecules is small (simulations #1 and #7 of Table 2), the amount of water in the simulation is not sufficient to observe the bulk spread of water on the surface. As the number of water molecules in the simulation decreases further, the layer connecting the silica surfaces becomes thinner and ultimately tears.

The contact angles of the water phase with hydroxylated silica in the vacuum and in the presence of gas are related to the surface tensions between various phases through Young's equations for the force balance at the meniscus. For the direction perpendicular to the silica surface

$$f_A = f_{wg} \sin \alpha \quad (4)$$

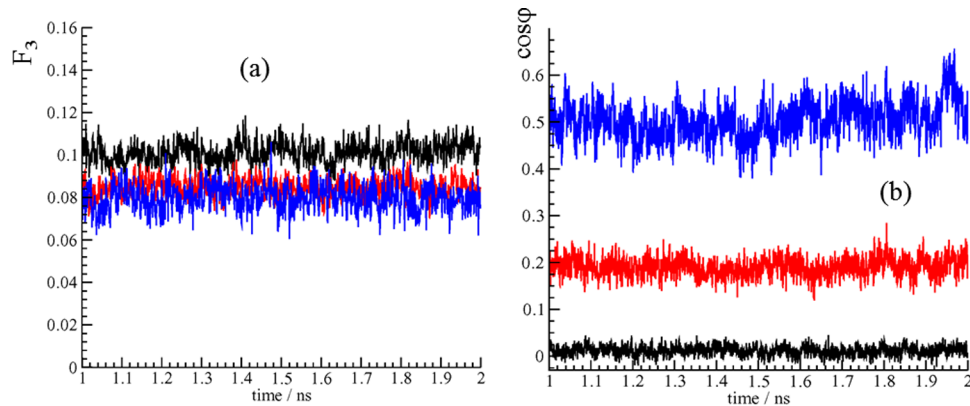


**Figure 8.** Typical orientation profiles for the water molecules (simulation 8): (a) the  $F_3$  parameter and (b) the angle  $\varphi$  between the polar moment vector of water and normal vector to the silica surface. The black lines are the  $L_1$  layer values, the red lines are the  $L_2$  layer values, and the blue lines are the C layer values.

where  $f_A$  is the adhesive force of the liquid water to the silica surface and  $f_{wg}$  is the tension force between the water and gas. For the direction parallel to the silica surface

$$f_{sw} + f_{wg} \cos \alpha = f_{sg} \quad (5)$$

where  $f_{sw}$  and  $f_{sg}$  are the tension forces between the solid silica–water and solid silica–gas phases, respectively. The latter equation is usually written in terms of the surface tensions

$$\gamma_{sw} - \gamma_{sg} = -\gamma_{wg} \cos \alpha \quad (6)$$

where the subscripts on the surface tension terms are similar to those of the tension forces. The silica–gas and water–gas interfacial tensions depend on the pressure of the gas in the simulation. In all simulations, we observe that the contact angle  $\alpha < 90^\circ$ , which implies that  $\gamma_{wg} > 0 > \gamma_{sw} - \gamma_{sg}$ . The contact angle increases as gas molecules are added to the water–silica systems, and this angle increases further at higher gas pressures, as seen in Table 2. As the gas pressure in the simulation increases, the interfacial tension force between the water and gas phases,  $f_{wg}$  in eq 4 decreases, requiring an increase in the contact angle  $\alpha$  to retain the force balance condition.

The ranges of contact angles at 300 K for the pure water–silica simulations (between 22 and 33°) are in good agreement with the experimental value of  $32.79 \pm 1.12^\circ$  reported by Skłodowska et al.<sup>46</sup> at 23 °C for distilled water on quartz.

**Order Parameter.** The local structure of the water phase was analyzed by studying the  $F_3$  parameter for layers of water oriented along the  $y$  direction. The  $F_{3,i}$  order parameters for oxygen atoms in each layer  $i$  averaged over the last 1 ns of the trajectory and are plotted in Figure 8a. The liquid water in the center of the meniscus has  $F_3 \approx 0.08$ . The order parameter for the  $L_2$  layer is slightly higher than the water in the center of the system. The order parameter  $L_1$  shows an average value of  $\sim 0.1$ , which implies a different hydrogen bonding network of the  $L_1$  layer compared with liquid water and ice, which is due to the orientation of the silica surface OH groups.

To understand the orientational characteristics of water molecules in these layers relative to the silica surface, we calculated and plotted in Figure 8b the average of the cosine of the angle,  $\varphi$ , between the dipole moment vector of water molecules and the normal vector of the silica surface,  $n$ , in Figure 4. The dipole moment vector of water molecules in the  $L_1$  layer appears to be approximately perpendicular (i.e.,  $\cos \varphi = 0$ ) to the silica surface. This indicates that one of the O–H groups of

water molecules in the  $L_1$  layer is predominantly arranged perpendicular to O–H groups of the silica surface. This is schematically shown in Figure 4. From Figure 8b, it is also evident that the water molecules in layer  $L_2$  ( $\cos \varphi \approx 0.2$ ) are oriented differently than the water molecules in the central, bulk-like C layer ( $\cos \varphi \approx 0.5$ ). We conclude that the orientational effect of the silica surface on the water molecules extends at least 6 Å into the water phase. This thickness for the bound layer is in good agreement with the finding of Handa et al.<sup>17</sup> who report a value between 4.5 to 5.5 Å from thermoporometric analysis of ice formation in porous Vycor glass and various silica gels with pore radii in the range 23–70 Å and with the study of Totland et al.<sup>47</sup> from their recent <sup>1</sup>H NMR relaxation time experimental results in silica samples (average diameter of 40 Å), where they reported the thickness of the affected water layer to be at least 8 Å.

**Residence Correlation Function.** This parameter is defined to investigate the dynamics and displacement of water molecules in each layer, and the results are plotted in Figure 9. The water molecules in layer  $L_1$  are noticeably less

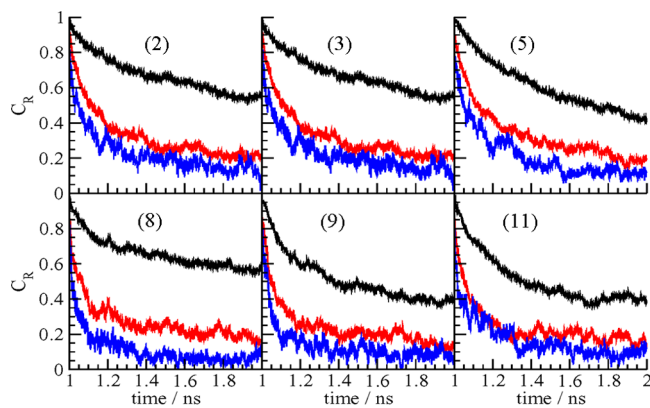


**Figure 9.** Residence correlation parameter for the water layers in the different simulations. The numbers in parentheses correspond to the simulation numbers in Table 2. The correlations for the  $L_1$  water layer adjacent to silica surface are shown in black, the correlations for  $L_2$  water layer are shown in red, and the correlations for the water layer in the center of the meniscus C are shown in blue. Top row is at 275 K and bottom row is at 300 K. The gas-phase space is empty for the left panel, filled with 306 methane molecules in the middle panel, and filled with 306 carbon dioxide molecules in the right panel.

mobile than those in layers L<sub>2</sub> and C. The water molecules in the L<sub>2</sub> are also less mobile than those of the C layer. As the temperature increases from 275 to 300 K, the rate of exchange of water between layers increases and C<sub>R</sub> decays faster. In the presence of gases, the mobility of the water molecules in L<sub>1</sub> increases. This suggests that the presence of CH<sub>4</sub> molecules in the gas space affects the dynamic behavior of water molecules in the L<sub>1</sub> layer. This could be due to the dissolution of gas molecules in the water phase and its hydrophobic nature (methane is nonpolar) as well as gas adsorption on the silica surface. Water is also spread out over a larger cross section of the surface at high temperature, which could affect its dynamics.

**Hydrogen Bond Analysis.** Because the water molecules in the hydrate structure are hydrogen-bonded, it is important to study how the silica surface and especially the surface O—H groups affect the hydrogen bonding dynamics of the adjacent water molecules. To assess the nature of hydrogen bonding between water molecules in the system, we calculated the intermittent hydrogen bond correlation functions (HBCFs) for water layers (L<sub>1</sub>, L<sub>2</sub>, and C). Water molecules in L<sub>1</sub> form hydrogen bonds with other water molecules as well as the O—H groups of the surface. These two contributions are separately computed and are labeled as C<sub>WW</sub> and C<sub>SW</sub>, respectively. Figure 10a shows the decay of HBCF for simulation 4. The surface

that the effect of silica surface extends to ~6 Å away from the surface, and water molecules beyond this distance behave similar to bulk water. An interesting phenomenon can happen in silica pores with diameter <12 Å, where bulk water would not be present.

## DISCUSSION

Our simulations show that the mobility of water molecules adjacent to the silica surface is significantly decreased, and as we move away from the surface, the behavior of the water molecules becomes more bulk-like. Methane and carbon dioxide molecules bind extensively to the liquid and silica surfaces.

These results suggest a heterogeneous nucleation mechanism for hydrates in porous media. Because relatively high guest/water molecule ratios are needed to form hydrates, the interfacial regions can deliver greater concentrations than delivered by gas solubility in water alone. The interface is an appropriate location for hydrate nucleation due to the enhanced relative concentration of gaseous guest molecules. The mobilities of water molecules in layers up to 6 Å away from the solid silica interface are also smaller than those in the bulk liquid phase, and this can further enhance the nucleation of clathrate hydrate phase. The entropy penalty for forming the solid hydrate from the less mobilized water near the surface is smaller than forming hydrate from bulk water molecules, which have full mobility of the liquid phase.

Yoslim et al.<sup>48</sup> studied the morphology of hydrate crystals and observed the formation of hydrates on the wall of the crystallizer above the gas (90.5% methane + 9.5% propane)/liquid interface where the gas and liquid phases were in contact with the solid surface of their reactor. The present simulations are consistent with these results. Because of the hydrophilic properties of the reactor, a thin layer of water forms on the wall. The hydrate-forming gas mixture is in contact with this thin water film and hydrate nucleated a few angstroms away from the solid surface of the reactor. The capillary that formed between the solid hydrate and the wall of the reactor served as the water supply channel to the reaction site and sustained further growth of the hydrate.

In contrast, Lehmkuhler et al.<sup>43</sup> used a sample cell with a water–gas (CO<sub>2</sub>) interface with no apparent contact of this interface with the wall of the containing cell. Under these conditions, some accumulation of CO<sub>2</sub> at the surface was observed, but no clathrate hydrate formation was detected. These results imply that the presence of the solid silica phase (container) can have an important effect on the hydrate formation mechanism for gas-phase guest molecules.

The average density profiles for H<sub>2</sub>O/CO<sub>2</sub> and H<sub>2</sub>O/CH<sub>4</sub> systems, particularly simulations 3 and 5, in the absence of silica surfaces as a function of the z coordinate are shown in Figure 7. The results of these simulations are in agreement with the experimental observations of Lehmkuhler et al.,<sup>43,44</sup> where enhanced concentration of CO<sub>2</sub> molecules was detected at the interface. It is evident that the solubility of CO<sub>2</sub> in water is larger than that of CH<sub>4</sub>. This indicates that the force field used predicts the behavior of the system qualitatively correctly. Also, near the interfacial layer, the relative concentration of the gas to H<sub>2</sub>O is significantly higher than that in the bulk water.

In Figure 1, three boxes with 7 × 7 Å<sup>2</sup> cross sections in the yz plane and a depth equal to the simulation box dimension in the x direction are selected. These distinct regions are shown as G (in gas phase), I (at the water–gas interface), and C (in water

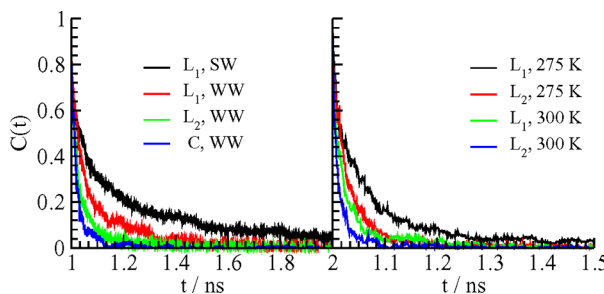


**Figure 10.** Intermittent hydrogen bond correlation function for water molecules in the L<sub>1</sub>, L<sub>2</sub>, and C layers.

water (SW) hydrogen bonding in L<sub>1</sub> has the slowest decay. This indicates that hydrogen bond formed between the silica surface and water molecules in L<sub>1</sub> is the most stable. The water–water (WW) HBCF in L<sub>1</sub> shows slower decay when compared with waters in L<sub>2</sub>, which shows that the silica surface indirectly affects the WW hydrogen bonding dynamics in L<sub>1</sub>. It also appears that this influence is extended to L<sub>2</sub>, although to a lesser extent. Figure 10b compares two similar simulations (5 and 11) at different temperatures. As expected, the simulation at higher temperature shows faster decay for HBCF as water molecules have greater kinetic energy, and hydrogen bonds break more quickly.

**Effect of Silica Layer Separation.** To assess whether the separation distance between the silica surfaces affects system properties, we performed two simulations (3a and 3b) with separations of 50 and 62 Å. These simulations were prepared such that their water/methane ratio is roughly the same as that in simulation 3 (separation distance of 38 Å). As reported in Table 2, the contact angles in these simulations are identical within the error margin of the measurements. Additionally, the F<sub>3</sub> order parameter, the C<sub>R</sub>(t) orientation parameter, the residence time, and the hydrogen bonding show similar trends for L<sub>1</sub>, L<sub>2</sub>, and C, which is assigned to be in the middle of the simulation box to represent the bulk water phase. This indicates

phase). The 7 Å distance is twice the distance of the first peak of OW–OW radial distribution function. The average number of water and gas molecules in the boxes during the final nanosecond of the simulation trajectories was counted and used to obtain the density of gases in each box. From the results of Table 3, it is clear that the local gas concentration at the interface (*I*) is considerably larger than the local gas concentration inside the gas phase (*G*). Therefore, as expected, the interface is more prone to nucleation of hydrates as compared with the bulk phase. As the number of gas molecules increases, the surface concentration enhancement becomes less pronounced and eventually disappears. The interface has a finite capacity to adsorb gas molecules and after reaching this limit additional gas molecules remain in the gas phase. Moreover, the concentration enhancement decreases at higher temperature, which shows that adsorption capacity of the interface becomes less with increasing temperature.

The average components of the system pressure tensor calculated from MD simulations for the equilibrated systems are given in Table 2. Comparing the components of the pressure tensor in the *x* and *z* directions, in contrast with the *y* direction (which is always negative), shows that there is considerable surface tension in the *y* direction in these simulations due to the presence of the meniscus. The surface tension may play an important role in the nucleation and capillary action of water in the hydrate-forming porous system. As expected, there are also correlations between the number of gas molecules in the simulation and the *x* and *z* components of the pressure tensor. These, in turn, affect the contact angle, such that larger contact angles are observed at higher gas pressures.

It should be noted that the pressure in this heterogeneous system is not uniform throughout the different phases and the expression for pressure tensor based on the virial only gives an overall view of pressure in this system. For example, the pressure in the gas phase should be relatively isotropic. The proper way of analyzing the pressure would be to consider each phase separately. Of particular interest would be the pressure across the gas–liquid interface for systems in vacuum and in systems with gases at different concentrations. Such a full analysis is beyond the scope of the present work and will be considered in the future simulations.

## CONCLUSIONS

We studied the distribution and dynamics of water molecules in a slit-like pore made up of fully hydroxylated silica surfaces in the absence and presence of hydrate forming gas molecules. Water molecules initially placed between the silica surfaces are allowed to evolve in an NVT ensemble simulation for 2 ns and form a meniscus (curved interface), confirming that silica is hydrophilic. The contact angle was determined by drawing tangents to the meniscus, and the results were in good agreement with the experimental values.

The water molecules at the silica surface are partially immobilized, and the hydrogen-bonding network is different from that of bulk water. Water molecules are preferentially populated near the O–H groups of silica surface, which indicates the formation of hydrogen bond between interfacial water molecules and the fully hydroxylated silica surfaces.

Methane and carbon dioxide are preferentially adsorbed on the water interface at the meniscus and at the surface of the exposed silica not wetted by water. We speculate that a possible nucleation site for heterogeneous nucleation of hydrates in

porous media is at the interfacial region between water phase and the hydrate forming gas and a few angstroms away from the solid surface immediately after the bound water layer (e.g., L<sub>2</sub> in our simulation), where the mobility of water molecules is slightly less than the bulk phase.

## ASSOCIATED CONTENT

### Supporting Information

Initial setup configurations for simulations 3 and 5, snapshots of CH<sub>4</sub> and CO<sub>2</sub> gas distribution adjacent to a flat water surface, and snapshot from simulations 3, 3a, and 3b after 2 ns showing the meniscus and methane gas phase for systems with silica layer separations of *y* = 62, 50, and 38 Å. This material is available free of charge via the Internet at <http://pubs.acs.org>.

## AUTHOR INFORMATION

### Corresponding Author

\*E-mail: englezos@chbe.ubc.ca; saman.alavi@nrc-cnrc.gc.ca; john.ripmeester@nrc-cnrc.gc.ca.

### Notes

The authors declare no competing financial interest.

## ACKNOWLEDGMENTS

We acknowledge Natural Resources Canada (NRCan) under the program “Gas Hydrates as a Canadian Energy Alternative” for partial funding of this research. The financial support of the Natural Sciences and Engineering Research Council of Canada and the computational support from the National Research Council of Canada are gratefully acknowledged.

## REFERENCES

- (1) Englezos, P. *Ind. Eng. Chem. Res.* **1993**, *32*, 1251–1274.
- (2) Gudmundsson, J. S. Method for Production of Gas Hydrates for Transportation and Storage. U.S. Patent No. 5,536,893, 1996.
- (3) Collett, T. S. *Am. Assoc. Pet. Geol. Bull.* **2002**, *86*, 1971.
- (4) Zatsepina, O.; Pooladi-Darvish, M. In *Canadian Unconventional Resources and International Petroleum Conference*, Calgary, Canada, 2010; SPE 137313.
- (5) Scharlin, P.; Battino, R. *J. Chem. Eng. Data* **1995**, *40*, 167–169.
- (6) Englezos, P.; Bishnoi, P. R. *Fluid Phase Equilib.* **1988**, *42*, 129–140.
- (7) Ripmeester, J. A.; Ratcliffe, C. I. *J. Phys. Chem.* **1988**, *92*, 337–339.
- (8) (a) Carroll, J. J.; Slupsky, J. D.; Mather, A. E. *J. Phys. Chem. Ref. Data* **1991**, *20*, 1201–1209. (b) Udachin, K. A.; Ratcliffe, C. I.; Ripmeester, J. A. *J. Phys. Chem. B* **2001**, *105*, 4200–4204.
- (9) Anderson, G. K. *J. Chem. Eng. Data* **2002**, *47*, 219–222.
- (10) Yamamura, K.; Fukuzaki, J.; Mori, Y. H. *Chem. Eng. Sci.* **2011**, *66*, 1844–1858.
- (11) Linga, P.; Haligva, C.; Nam, S. C.; Ripmeester, J. A.; Englezos, P. *Energy Fuels* **2009**, *23*, 5496–5507.
- (12) (a) Seo, Y. T.; Moudrakovski, I. L.; Ripmeester, J. A.; Lee, J.; Lee, H. *Environ. Sci. Technol.* **2005**, *39*, 2315–2319. (b) Bagherzadeh, S. A.; Moudrakovski, I. L.; Ripmeester, J. A.; Englezos, P. *Energy Fuels* **2011**, *25*, 3083–3092.
- (13) Riedel, M.; Collett, T.; et al. *EOS, Trans. Am. Geophys. Union* **2006**, *87*, 325.
- (14) (a) Argyris, D.; Tummala, N. R.; Striolo, A.; Cole, D. R. *J. Phys. Chem. C* **2008**, *112*, 13587–13599. (b) Luzar, A.; Chandler, D. *Nature* **1996**, *379*, 55–57.
- (15) Aines, R. D.; Rossman, G. R. *J. Geophys. Res.* **1984**, *89*, 4059–4071.
- (16) Konrad, J.-M. *Cold Reg. Sci. Technol.* **1990**, *18*, 49–55.
- (17) Handa, Y. P.; Zakrzewski, M.; Fairbridge, C. *J. Phys. Chem.* **1992**, *96*, 8594–8599.

- (18) Ping, Z. H.; Nguyen, Q. T.; Chen, S. M.; Zhou, J. Q.; Ding, Y. D. *Polymer* **2001**, *42*, 8461–8467.
- (19) Anderson, D. M. *J. Colloid Interface Sci.* **1967**, *25*, 174–191.
- (20) Razul, M. S.; Tam, E. V.; Lam, M. E.; Linden, P.; Kusalik, P. G. *Mol. Phys.* **2005**, *103*, 1929–1943.
- (21) Vatamanu, J.; Kusalik, P. G. *J. Chem. Phys.* **2007**, *126*, 124703–124703.
- (22) Walsh, M. R.; Koh, C. A.; Sloan, E. D.; Sum, A. K.; Wu, D. T. *Science* **2009**, *326*, 1095.
- (23) Liang, S.; Kusalik, P. G. *Chem. Phys. Lett.* **2010**, *494*, 123–133.
- (24) Vatamanu, J.; Kusalik, P. G. *Phys. Chem. Chem. Phys.* **2010**, *12*, 15065–15072.
- (25) Bai, D.; Chen, G.; Zhang, X.; Wang, W. *Langmuir* **2011**, *27*, 5961.
- (26) Vatamanu, J.; Kusalik, P. G. *J. Phys. Chem. B* **2006**, *110*, 15896–15904.
- (27) Smith, W.; Forester, T. R. *J. Mol. Graphics* **1996**, *14*, 136–141.
- (28) Tse, J. S.; Klein, M. L.; McDonald, I. R. *J. Phys. Chem.* **1983**, *87*, 4198–4203.
- (29) Harris, J. G.; Yung, K. H. *J. Phys. Chem.* **1995**, *99*, 12021–12024.
- (30) Abascal, J. L. F.; Sanz, E.; Fernández, R. G.; Vega, C. *J. Chem. Phys.* **2005**, *122*, 234511.
- (31) Lopes, P. E.; Murashov, V.; Tazi, M.; Demchuk, E.; MacKerell, A. D., Jr. *J. Phys. Chem. B* **2006**, *110*, 2782–2792.
- (32) Walsh, M. R.; Koh, C. A.; Sloan, E. D.; Sum, A. K.; Wu, D. T. *Science* **2009**, *326*, 1095–1098.
- (33) Bai, D.; Chen, G.; Zhang, X.; Wang, W. *Langmuir* **2012**, *28*, 7730–7736.
- (34) Anderson, B. J.; Tester, J.; Trout, B. *J. Phys. Chem. B* **2004**, *108*, 18705–18715.
- (35) Sun, R.; Duan, Z. *Geochim. Cosmochim. Acta* **2005**, *69*, 4411–4424.
- (36) Mastny, E. A.; Miller, C. A.; de Paulo, J. J. *J. Chem. Phys.* **2008**, *129*, 034701.
- (37) Velaga, S.; Vedam, V.; Anderson, B. J. In *Proceedings of the 7th International Conference on Gas Hydrates*; Edinburg, Scotland, U.K., 2011.
- (38) Levien, L.; Prewitt, C. T.; Weidner, D. *J. Am. Mineral.* **1980**, *65*, 920.
- (39) Bagherzadeh, S. A.; Englezos, P.; Alavi, S.; Ripmeester, J. A. *J. Phys. Chem. B* **2012**, *116*, 3188–3197.
- (40) Saville, G. *J. Chem. Soc., Faraday Trans. 2* **1977**, *73*, 1122–1132.
- (41) Nijmeijer, M. J. P.; Bruin, C.; Bakker, A. F.; van Leeuwen, J. M. *J. Physica A* **1989**, *160*, 166–180.
- (42) Baez, L. A.; Clancy, P. *Ann. N.Y. Acad. Sci.* **1994**, *715*, 177–186.
- (43) Boewer, L.; Nase, J.; Paulus, M.; Lehmkühler, F.; Tiemeyer, S.; Holz, S.; Pontoni, D.; Tolan, M. *J. Phys. Chem. C* **2012**, *116*, 8548–8553.
- (44) Lehmkühler, F.; Paulus, M.; Sternemann, C.; Lietz, D.; Venturini, F.; Gutt, C.; Tolan, M. *J. Am. Chem. Soc.* **2008**, *131*, 585–589.
- (45) Chen, F.; Smith, P. E. *J. Chem. Phys.* **2007**, *126*, 221101.
- (46) Skłodowska, A.; Matlakowska, R. *Biotechnol. Tech.* **1997**, *11*, 837–840.
- (47) Totland, C.; Steinkopf, S.; Blokhus, A. M.; Nerdal, W. *Langmuir* **2011**, *27*, 4690–4699.
- (48) Yoslim, J.; Linga, P.; Englezos, P. *J. Cryst. Growth* **2010**, *313*, 68–80.